Fuel 427 (2027) 139812

Contents lists available at ScienceDirect

Fuel

journal homepage: www.elsevier.com/locate/fuel

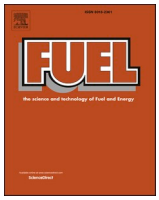

Full Length Article

Cobalt doping as a microstructural optimization strategy for $Sr_2Fe_{1.5}Mo_{0.5}O_{6-\delta}$ cathodes in direct ammonia SOFCs for N_2O abatement

Celina Fernandes [a,b], Laura I.V. Holz [c,d], Francisco J.A. Loureiro [c,d], Sergey M. Mikhalev [c,d], Duncan P. Fagg [c,d], Adélio Mendes [a,b,*]

[a] LEPABE – Laboratory for Process Engineering, Environment, Biotechnology and Energy, Faculty of Engineering, University of Porto, Rua Dr. Roberto Frias, 4200-465 Porto, Portugal
[b] ALiCE – Associate Laboratory in Chemical Engineering, Faculty of Engineering, University of Porto, Rua Dr. Roberto Frias, 4200-465 Porto, Portugal
[c] TEMA - Centre for Mechanical Technology and Automation, Department of Mechanical Engineering, University of Aveiro 3810-193 Aveiro, Portugal
[d] LASI - Intelligent Systems Associate Laboratory, 4800-058 Guimarães, Portugal

ARTICLE INFO

Keywords:
Solid Oxide Fuel Cell (SOFC)
Cathode
$Sr_2Fe_{1.5}Mo_{0.5}O_{6-\delta}$ (SFMO)
Cobalt doping
Nitrous oxide abatement
Ammonia

ABSTRACT

Perovskite-type oxides are promising materials for mitigating nitrous oxide (N_2O) emissions. Although widely studied for thermal N_2O decomposition, their application in electrochemical N_2O abatement in solid oxide fuel cells (SOFCs) remains largely unexplored. The double perovskite $Sr_2Fe_{1.5}Mo_{0.5}O_{6-\delta}$ (SFMO) stands out for its mixed ionic–electronic conductivity and redox stability; however, it exhibits low power conversion efficiency when N_2O is supplied to the cathode. This work focuses on improving SFMO performance by partially substituing Fe with small amount of Co ($Sr_2Fe_{1.5-x}Co_xMo_{0.5}O_{6-\delta}$, $x = 0.05$) to enhance its intrinsic and microstructural properties, aiming to improve cathode performance under N_2O conditions in a direct ammonia SOFC (DA-SOFC), operating at 600–750 °C.

Electrochemical impedance spectroscopy revealed similar reaction mechanisms in both compositions, despite notable microstructural differences caused by Co-doping. The denser SFCMO layers showed better grain connectivity, nearly doubling the peak power density (~30 mW cm^{-2}) compared to undoped SFMO, highlighting the beneficial role of microstructural alterations.

1. Introduction

Nitrous oxide (N_2O) is the third most important long-lived greenhouse gas after CO_2 and CH_4, contributing to global warming, acid rain formation and ozone layer depletion [1]. Its major anthropogenic sources include nitric and adipic acid production, food production, and burning fossil fuels [2]. Reducing N_2O emissions is therefore of great importance and is typically achieved by catalytic reduction [2]. Although this process is efficient, it often relies on noble-metal-based catalysts, which results in high costs [2]. In addition, it has been widely reported that the removal of oxygen species formed during N_2O decomposition at active sites can act as a rate-limiting step, further hindering reaction kinetics [3]. Therefore, its continuous consumption would effectively overcome this limitation, and facilitate the regeneration of surface-active sites and enable process intensification, thereby greatly promoting N_2O conversion [3].

In this context, solid oxide fuel cells (SOFC), particularly, direct ammonia SOFCs (DA-SOFCs), in which N_2O decomposition and oxygen reduction reaction (ORR) are coupled in the cathode, represent a promising alternative for N_2O mitigation. Owing to their fuel flexibility and resistance to poisoning, DA-SOFC can simultaneously reduce N_2O while converting the chemical energy of a fuel (NH_3) into electrical energy and useful value-added chemicals [4,5].

DA-SOFC has gained attention because NH_3 can serve as a carbon-free hydrogen carrier. Compared with H_2, NH_3 offers several advantages, including easier liquefaction, higher volumetric energy density, and safer storage and transportation [6]. When operated with N_2O as the oxidant, nitric oxide (NO) may be produced, a valuable intermediate for nitric acid synthesis, thereby contributing to decarbonization and circular economy strategy [7]. However, N_2O abatement in SOFC or DA-SOFC remains scarcely reported in literature, particularly regarding the limited understanding of the kinetics of N_2O reduction mechanism at the cathode, where N_2O is reduced to N_2 and O_2 and strongly depends on operating temperature.

SOFCs operates at high temperatures (800–1000 °C), which enhance electrochemical activity; however, this condition imposes constraints on

* Corresponding author.

https://doi.org/10.1016/j.fuel.2026.139812
Received 13 March 2026; Received in revised form 23 April 2026; Accepted 6 May 2026
Available online 16 May 2026

material selection and long-term operation [5]. Therefore, intermediate operating temperatures (600–750 °C) have become an important target to balance performance and stability [8]. At these temperatures, however, sluggish kinetics of the oxygen reduction reaction (ORR) increases polarization resistance, which remains a major contributor to overall SOFC performance losses [5], and highlight the need for stable and highly electroactive cathode materials that must combine catalytic activity and efficient charge transport [6].

Among candidate materials, mixed ionic-electronic conducting (MIEC) perovskites have emerged as leading cathode options [9]. In particular, the double perovskite $Sr_2Fe_{1.5}Mo_{0.5}O_{6-\delta}$ (SFMO) exhibits strong redox activity and stability, along with excellent electronic (~20 S cm^{-1}) and oxide-ion (~ 0.13 S cm^{-1} at 800 °C) conductivities [10,11]. However, its overall efficiency under an N_2O cathodic atmosphere was insufficient, particularly due to the low Faradaic efficiency observed [12]. To enhance performance, the cathode material should exhibit a higher concentration of oxygen vacancies and improved electrocatalytic activity [11]. Cation substitution is widely used as a strategy to enhance the properties of perovskites electrodes. In particular, cobalt substitution at the B-site of SFMO increases the fraction of tetravalent cations, enhances oxygen mobility and reduction activity, and stabilizes the cubic symmetry at room temperature, in association with higher oxygen content [13,14]. All these characteristics can favour redox surface reactions and potentially reduce polarization resistance in electrochemical systems [15], which are critical variables in the electrochemical decomposition of nitrous oxide [16,17]. Co substitution is also reported to modify Fe/Mo valence distribution, optimizing the Fe^{3+}/Fe^{4+} and Mo^{5+}/Mo^{6+} ratios, which often leads to improved electrocatalytic activity and stability [11,13]. However, these effects have primarily been reported under conventional SOFC operating conditions, and their impact under N_2O-containing atmospheres combined with NH_3 feeding remains unclear.

The poor performance of SFMO may also be related to the limited flexibility in optimizing its microstructure due to constraints on applying high sintering temperatures. Insufficient densification resulting from these temperature limitations can compromise intergranular contact, electrode–electrolyte adhesion, and porosity optimization, thereby increasing polarization losses despite the intrinsically favorable electronic and ionic properties of the material [18]. Improving the microstructure of SFMO is challenging because, at relatively low temperatures (~1000 °C), Sr can react with the YSZ electrolyte to form strontium zirconate, a highly insulating phase [19,20]. This challenge can be mitigated by using a CGO buffer layer. However, at temperatures above 1200 °C, CGO is also reported to react with YSZ, which prevents significant increases in the sintering temperature for electrode fabrication and, consequently, limits straightforward thermally driven microstructural tailoring [21,22]. These limitations highlight the need for alternative strategies to tailor microstructure without increasing sintering temperature. Doping the SFMO electrode with Co may also play a secondary role, as it can induce microstructural changes without the need for high sintering temperatures, given that Co is well known as a sintering aid in perovskite-related materials [23].

Building on this insight, the main objectives of the present study are to exploit Co as a means to tailor the intrinsic electrical properties of SFMO, and thereby its electrocatalytic performance, and as a potential sintering aid to improve its microstructure. While Co doping has been widely explored in SOFC materials, its role in enabling simultaneous microstructural optimization and electrochemcial performance under N_2O-containing atmospheres, combined with direct NH_3 fuel feeding, remains largely unexplored. In addition, strategies that improve electrode performance without requiring high-temperature processing are particularly relevant for Sr- and Y-containing systems where thermal constrains limit conventional microstructural optimization approaches. To the best of the authors' knowledge, studies combining Co-doped SFMO-type materials with N_2O – containing atmospheres and direct NH_3 fuel feeding remain very limited, highlighting the novelty of the present approach.

The present work, therefore, demonstrates that the use of low level of Co doping ($x = 0.05$) in $Sr_2Fe_{1.5}Mo_{0.5}O_{6-\delta}$ (SFMO), forming SFCMO ($Sr_2Fe_{1.5-x}Co_xMo_{0.5}O_{6-\delta}$), can simultaneously improve microstructure and electrochemical performance under challenging cathodic N_2O atmosphere in a DA-SOFC operating at intermediate temperatures (600–750 °C). This approach provides an effective strategy to enhance electrode performance without relying on high-temperature processing. A comparative analysises between the SFMO and SFCMO is presented, offering valuable insights into the relationships between microstructure, catalytic activity, and electrocatalytic performance in SFMO-based perovskites, thereby contributing to the development of efficient and stable cathodes for N_2O Electrochemical behavior was assessed through polarization measurements and electrochemical impedance spectroscopy (EIS).

2. Materials and methods

2.1. Catalyst preparation

The $Sr_2Fe_{1.5-x}Co_xO_{6-\delta}$ particles (with $x = 0$, referred to as SFMO and $x = 0.05$, referred to as SFCMO) were synthesized via sol–gel method [14]; The Co substitution level ($x = 0.05$) was selected as it provides a suitable balance between an optimal Goldschmidt tolerance factor and thermomechanical compatibility with other cell components, while avoiding structural instability and the formation of secondary phases at higher Co content [24].

Stoichiometric amounts of strontium nitrate, iron nitrate, and cobalt nitrate (Sigma-Aldrich, purity > 99 %), as well as ammonium molybdate (Sigma-Aldrich, purity > 99 %), were dissolved in distilled water. Ethylenediaminetetraacetic acid (EDTA) was first dissolved in an aqueous ammonia solution (25 %) and subsequently added to the nitrate solution, where it served as a gelling agent. The molar ratio of EDTA to total metal ions was 1.5:1. The pH of the solution was adjusted to 10 by the addition of aqueous ammonia under continuous stirring. The mixture was heated to 90 °C, yielding black precursor gels. The resulting powder was calcined at 800 °C for 2 h using heating and cooling rates of 3 °C min^{-1}. The calcined product was then ground in an agate mortar, pressed into pellets, and subjected to a second calcination step at 1200 °C for 10 h to ensure phase formation and chemical homogeneity.

X-ray diffraction (XRD) analyses were performed using a *Rigaku SmartLab* diffractometer (Cu K_α radiation – 1.5406 Å, 40 kV, 30 mA). Diffraction patterns were collected over 2θ range between 20° and 80°, at a scan rate of 3 °C min^{-1}. Rietveld refinement was carried out to determine the lattice parameters, employing a pseudo-Voigt peak profile function for the peak fitting and a B-spline function to model the background.

X-ray photoelectron spectroscopy (XPS) was employed to characterize the surface of the cobalt-containing electrocatalyst (SFCMO), specifically to determine the presence of cobalt at the perovskite surface and its oxidation state. The analysis was performed using a SPECS spectrometer equipped with a Phoibos 150 MCD-9 detector and a non-monochromatic Mg K_α X-ray source. The XPS spectra were collected under a vacuum pressure of 10^{-9} mbar, employing a pass energy of 20 eV and an X-ray power output of 300 W. SFMO was also analysed by XPS, and in this case, XPS spectra were acquired in an Ultra High Vacuum (UHV) system with a base pressure of 2 x 10^{-10} mbar. The system is equipped with a hemispherical electron energy analyser (SPECS *Phoibos* 150), a delay-line detector, and a monochromatic AlK_α (1486.74 eV) X-ray source. High-resolution spectra were recorded at a normal emission take-off angle and with a pass energy of 10 eV, which provides an overall instrumental peak broadening of 0.5 eV. Data processing involved the utilization of CASA XPS software, with Shirley-type background correction.

Produced particles were analysed by Scanning Electron Microscopy (SEM), FEI QUANTA 400 FEG ESEM / EDAX PEGASUS to evaluate the

morphology and particle size of the obtained powders. The microscope was operated at an applied potential difference of 15 kV, with a back-scattered electron (BSE) detector and secondary electrons.

Thermogravimetric analysis (TGA) was conducted on a *NETZSCH TG 209* instrument under synthetic air up to 1150 °C, with a heating rate of 5 °C min^{-1} and a dwell time of 1 h at the final temperature. The sinterability curves of each prepared catalyst were obtained by using a dilatometer L75 Horizontal *Linseis* over a temperature range between 21 °C and 1200 °C.

The textural properties of each sample were evaluated by N_2 physisorption (196 °C) in a Quantachrome Autosorb-1 Instruments device. The surface area (S_{BET}) was obtained from the Brunauer-Emmett-Teller (BET) equation for a nitrogen partial pressure range of (p/p_0) from 0 to 1. The samples (*ca.* 120 mg) were outgassed in a vacuum at 200 °C for 4 h.

2.2. Fabrication of the membrane electrode assembly (MEA)

The present work employed a commercial anode-supported half-MEA (Elcogen), with 35 mm diameter, consisting of a Ni/YSZ anode and a Gadolinia-doped Ceria buffer layer ($Ce_{0.8}Gd_{0.2}O_{2-\delta}$ – CGO20). The anode comprised the three functional layers with a total thickness of approximately 300 μm: the active fuel electrode layer of Ni/8YSZ $(ZrO_2)_{0.92}(Y_2O_3)_{0.08}$, the support layer of Ni/3YSZ $(ZrO_2)_{0.97}(Y_2O_3)_{0.03}$ and the contact layer of NiO. Each cathode was deposited by screen-printing an ink containing the synthesized perovskite powders: SFMO and SFCMO on top of the CGO20 buffer layer. Each ink was prepared by mixing the perovskite powder with a solution of 95 wt% of terpineol with 5 wt% of ethyl cellulose in a 20:80 vol% (powder: solution) ratio. Stearic acid (3 wt%) was added as a dispersant to the mixture. All the compounds were ground in an agate mortar for 15 min to obtain a homogeneous slurry. The cathode was applied in two screen-printed layers, followed by thermal treatment at 350 °C for 1 h to remove the organic binders, and sintering at 1000 °C for 4 h in air using a heating and cooling rate of 1.5 °C min^{-1}. The resulting working electrode areas were 1.51 cm^2 for SFMO and 1.08 cm^2 for SFCMO. Fig. 1 shows a schematic representation of the 2-probe cell used for the present study.

Afterwards, the cell was assembled into an in-house-made electrochemical reactor; the sample was sealed with glass (Glass Powder G018-354 from SCHOTT) in a Crofer 22 APU support and thermally sintered using the following sealing procedure: 350 °C for 30 min, followed by 850 °C for 1 h, with a heating/cooling ramp of 2 °C min^{-1}. A gold grid (from Fiaxell) was used as a current collector on both the cathodic and anodic sides of the single cell.

2.3. Catalytic experiments

The chemical reaction catalytic experiments were carried out in a fixed-bed reactor. Catalyst samples were placed in an AISI 316 stainless steel reactor (50 mm length and 7.8 mm inner diameter), filled with silica beads (212–300 μm), with a middle layer of 0.5 g of catalyst for the catalytic run. The reactor temperature was maintained using a PID-controlled vertical furnace. N_2O was fed to the top of the reactor at different feed flow rates (15, 40, 80, and 130 mL min^{-1}), corresponding to Gas Hourly Space Velocity (GHSV) of 4500, 12 000, 24 000, and 39 000 h^{-1}, respectively, within a temperature range of 540–750 °C; GHSV was calculated as the ration between volumetric flow rate of N_2O and volume of the catalyst bed.

Product gas samples were acquired after 50 min, to ensure a steady state operation, and the gas samples were analysed using a gas chromatograph (Agilent 7890B) equipped with a PoraPlot Q column to analyze N_2O, and a 5Å Molsieve column to analyze N_2 and O_2. The N_2O used in this work has a purity of $>$ 99.5 %, O_2 $>$ 99.9995 %.

2.4. Electrocatalytic experiments

Electrochemical Impedance Spectroscopy (EIS) and current–potential difference (*I-V*) characteristics of every single cell were carried out using an *Autolab* PGSTAT302 N potentiostat. The reactor was fed with NH_3 (fuel, 50 mL min^{-1}) at the anode and with N_2O (oxidant, 50 mL min^{-1}) at the cathode. Measurements were conducted over a temperature range of 600–750 °C, starting with the highest temperatures. The EIS spectra were recorded over the frequency range of 0.01 Hz to 1 MHz using an amplitude of 50 mV, at different polarization potentials (−0.2, −0.4, −0.6, −0.8, −1.0 V). To ensure equilibrium conditions, each temperature point was stabilized for 1h prior to recording the EIS spectrum, followed by a repeat scan after an additional hour under identical conditions, to assess reproducibility.

The impedance data were analysed using non-linear least-squares fitting in ZView© software (Scribner Associates), employing appropriate equivalent circuit models to identify the resistive and capacitive contributions of the individual electrochemical processes. The NH_3 and N_2O gases (Air Liquide) supplied to the cell had a purity of $>$ 99.996 % and of $>$ 99.5 %, respectively.

After the electrochemical experiments, the microstructure of a fractured cross-section of a membrane electrode assembly (MEA) was analysed by Scanning Electron Microscopy (SEM), *Hitachi TM4000 plus*. The microscope was operated using an applied voltage of 15 kV, using a Backscattered Electron (BSE) detector. Energy dispersive X-ray analysis

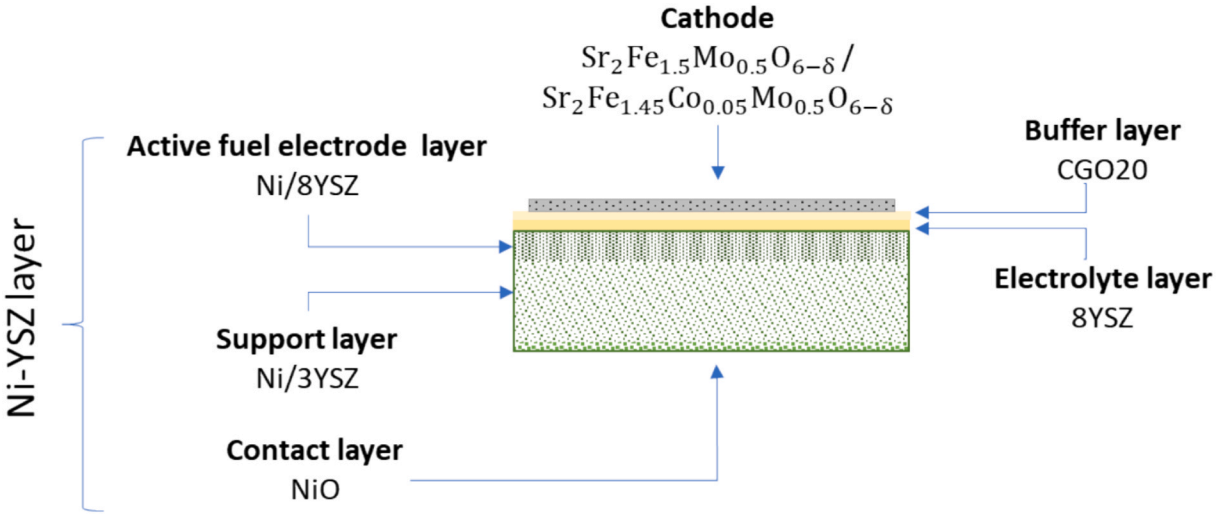

Fig. 1. Schematic representation of the membrane electrode assembly: SFMO/SFCMO||CGO||YSZ||Ni-YSZ.

(EDS) was performed to provide the elemental mapping of the samples. X-ray diffraction (XRD) was performed to structurally characterize the materials of this work, using a *Rigaku SmartLab* diffractometer (Cu Kα radiation – 1.5406 Å, 40 kV, 30 mA). The patterns were obtained in the range of $10° < 2\theta < 90°$, scan speed of 3 °C min $^{-1}$.

3. Results and discussion

3.1. Structural characterization

Fig. 2 presents the SEM images of the synthesized catalysts. The SFMO catalyst (Fig. 2 **a)**) exhibits faceted morphology with an average particle size of *ca.* 0.68 ± 0.11 μm. In contrast, Co-doped SFMO sample (Fig. 2 **b)**) displays a more irregular, flake-like morphology and small average particle size of *ca.* 0.21 ± 0.03 μm. However, a higher degree of agglomeration is observed in the doped catalyst compared to the undoped SFMO catalyst.

Fig. 3 portraits the XRD pattern of the $Sr_2Fe_{1.5}Mo_{0.5}O_{6-\delta}$ (SFMO) and $Sr_2Fe1_{.45}Co_{0.05}Mo_{0.5}O_{6-\delta}$ (SFCMO) obtained after calcination of the prepared powders at 1200 °C. Results indicated a pure phase for both catalysts. The XRD data were analyzed by Rietveld refinement, indicating that the two prepared catalysts exhibit cubic symmetry ($Fm\bar{3}m$ space group).

Table 1 depicts the lattice parameters obtained by Rietveld refinement for each catalyst – $a = b = c = 7.8395(1)$ and 7.8368(8) Å for SFMO and SFCMO, respectively. The slight reduction in the lattice parameter observed in the perovskite doped with Co is consistent with substitutional incorporation of Co at the Fe site and a change in the average B-site ionic radius (Fe^{3+} for VI coordination has 0.785 Å while Co^{3+} has 0.75 Å) [25], leading to a small shift of the peaks to higher 2θ. The low χ^2 value ~ 1 (Table 1) of the Rietveld refinement analysis indicates a good quality of the fitting ($\chi^2 = R_{wp}/R_{exp}$, where R_{wp} (profile *R*-factor) and R_{exp} (expected *R*-factor based on statistical noise) are statistical factors) for both perovskites display a good fit.

A thermogravimetric analysis (TGA) was performed to quantify the lattice oxygen loss resulting from the reduction of metal ions during heating in dry air. Fig. 4 shows the overall mass loss during the heating of the two prepared samples. SFMO had a mass loss of about 2.0 %, while SFMO cobalt-doped showed a slightly higher value of 2.2 %. In both cases, the observed mass loss was attributed to oxygen release and the consequent formation of oxygen vacancies, which has been suggested in the literature to arise from the reduction of cationic species and the possible formation of Fe^{4+}/Fe^{3+}, Mo^{6+}/Mo^{5+}, and – in the case of the doped cathode – Co^{2+}/Co^{3+} redox couples for charge compensation [9]. The slight initial mass above 100 % in case of SFMO is attributed to typical TGA artifacts, such as buoyancy effects and minor baseline drift at low temperatures.

The accelerated mass loss observed in SFCMO in the 600–800 °C temperature range, compared with the more linear mass loss of SFMO, can be attributed to Co substitution at the B-site of the double-perovskite structure. This substitution has been reported to modify the redox activity of this perovskite, thereby promoting enhanced oxygen release from the lattice at elevated temperatures when cobalt is present [15,26].

The corresponding oxygen stoichiometry changes were calculated for both tested materials, using the following Eq. (1) [27]:

$$\Delta\delta = \frac{M_{SFMO/SFCMO}}{M_O . w_{sample}} . \Delta w \quad (1)$$

where $\Delta\delta$ is the oxygen stoichiometry change, $M_{SFMO/SFCMO}$ is the molecular mass of SFCMO/SFCMO, M_O is the atomic mass of oxygen, w_{sample} is the mass of the sample, and Δw is the mass change recorded by the TGA. The calculations indicate that substituting Fe with a small amount of Co in the SFMO ($x = 0.05$) results in a slight increase in oxygen stoichiometry, with $\Delta\delta$ increasing from 0.50 for SFMO to 0.55 for SFCMO on heating to 1000 °C. This indicates that even minor Co substitution promotes the formation of oxygen vacancies at high temperatures, likely as a charge-compensating mechanism associated with local changes in Fe/Mo valence states. Although the magnitude of this increase is relatively small, it may be sufficient to influence the catalytic and electrocatalytic properties of the material in the working temperature range [11,13], without compromising structural stability.

Dilatometry was employed to assess the sinterability of the prepared perovskites. The resulting shrinkage curves and their derivatives – Fig. 5 **a)** and Fig. 5 **b),** respectively – provide insight into the densification behavior of the catalysts.

As observed, the Co-doped SFMO starts to contract and densify at lower temperatures than the undoped material. Specifically, SFCMO begins to shrink at *ca.* 969 °C, while SFMO starts contracting about 70 °C later, at around 1031 °C, Fig. 5 **b)**. These results indicate that Co substitution on B-site in SFMO promotes its sintering, enabling densification to occur at lower temperatures without the need to increase the sintering temperature above 1200 °C.

3.2. Catalytic experiments

Fig. 6 presents the results of the catalytic experiments performed over particulated SFMO and SFCMO samples. Fig. 6 **a)** and Fig. 6 **b)** show the catalytic conversion of N_2O for the studied temperatures in the range of 600 to 750 °C, respectively, after correcting for the homogeneous thermal decomposition of N_2O measured in a blank experiment (without catalyst), presented in Fig. 6 **c)**.

The conversion of N_2O (X_{N_2O}) to N_2 and O_2, according to:

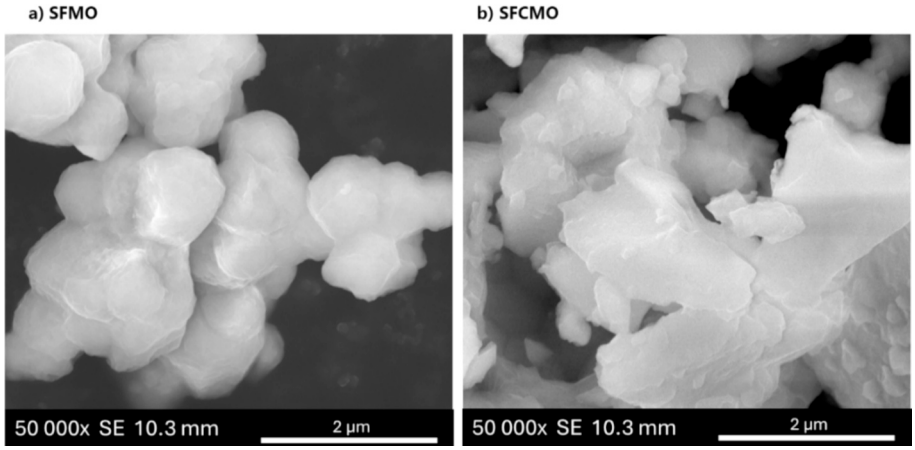

Fig. 2. Scanning electron microscopy (SEM) of the synthesised catalysts (a) SFMO and (b) SFCMO.

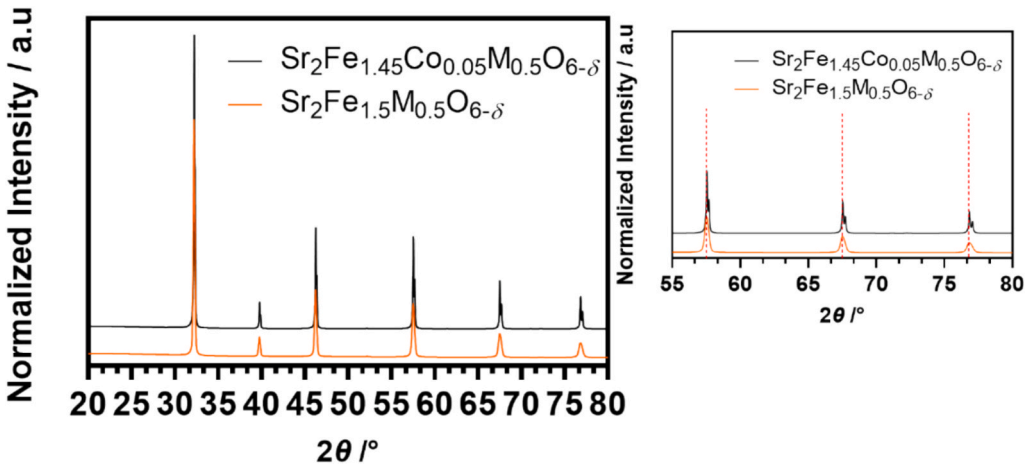

Fig. 3. XRD pattern with Rietveld refinement analysis of SFMO and SFCMO cathodes obtained under air atmosphere after calcination at 1200 °C.

Table 1
Rietveld refinement extracted parameters of SFMO and SFCMO. R_{wp}, R_{exp}, χ^2, and S are statistical factors of Rietveld refinement quality.

Material	SFMO	SFCMO
Space Group	$Fm\bar{3}m$(Cubic symmetry)	$Fm\bar{3}m$(Cubic symmetry)
Lattice parameter ($a = b = c$) / Å	7.8395(1)	7.8368(8)
Phase angle ($\alpha = \beta = \psi$) / °	90.0	90.0
R_{wp} / %	3.86	3.76
R_{exp} / %	3.04	2.85
χ^2	1.2759	1.3905
S	1.5659	1.1792

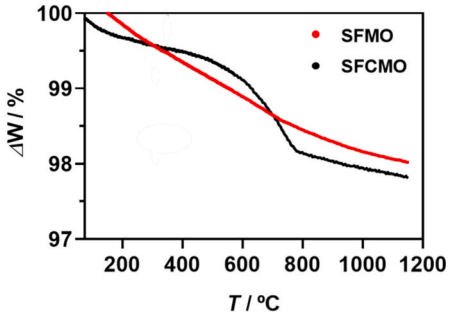

Fig. 4. Thermogravimetry results of the (a) SFMO and (b) SFCMO in air.

$$N_2O\,(g) \rightarrow N_2\,(g) + O_2\,(g) \Delta H^0 = -82.05\,kJ\,mol^{-1} \quad (2)$$

was computed as:

$$X_{N_2O} = \frac{Q_{N_2O\ in} - Q_{N_2O\ out}}{Q_{N_2O\ in}} \quad (3)$$

where $Q_{N_2O\ in}$ is the inlet molar flow, and $Q_{N_2O\ out}$ is the outlet molar flow from the reactor.

Overall, SFMO exhibits superior performance, achieving conversion values of 42 % and 48 %, at a feed flowrate of 130 mL min^{-1}, for 750 °C and 650 °C, respectively. Under the same conditions, the cobalt-doped catalyst (SFCMO) displayed a lower N_2O conversion of 31 % and 27 %, respectively.

The temperature required for 50 % N_2O conversion (T_{50}) is 650 °C for both perovskites, which is consistent with literature reports for Fe-containing perovskite-types oxides under comparable conditions [28,29]. Notably, the undoped perovskite can achieve T_{50} at a higher flow rate (80 mL min^{-1} for SFMO *vs* 15 mL min^{-1} for SFCMO), indicating greater tolerance to increased gas space velocity. However, while the maximum conversion of 68 % for SFMO was reached for 700 °C, if the reactor is heated to 750 °C, the N_2O conversion 63 %. Concerning the SFCMO catalyst slab, the maximum conversion is 60 % at 700 °C and roughly the same at 750 °C.

Overall, the observed conversion values (*e.g.* 42–48 % at T_{50} ~ 650 °C and GHSV ~ 24 000 h^{-1}) indicate moderate catalytic activity compared with literature reports for perovskite-type oxides [28,30,31]. Such behaviour is often correlated with the presence of redox-active surface metal species that facilitate electron transfer to the adsorbed N_2O molecule and promote N-O bond cleavage [15]. The influence of the feed gas flow rate is particularly evident: lower flow rates (*e.g.*, lower gas hourly space velocity, GHSV) allow for higher conversion. In general, higher temperatures also promote catalyst activity, namely, the cleavage of the N-O bond.

Subsequently, these results were normalized by the BET surface area of the catalyst powders, according to Eq. (4):

$$r = \frac{X_{N_2O} \times Q_{N_2O\ in}}{w_{sample} \times S_{BET}} \quad (4)$$

where X_{N_2O} is N_2O conversion, $Q_{N_2O\ in}$ is the inlet molar flow in the reactor, w is the used mass of catalyst (g) and S_{BET} is the BET surface area – 7.086 and 12.943 $m^2\,g^{-1}$for SFMO and SFCMO, respectively; the SFMO pore volume was determined to be 0.015 $cm^3\,g^{-1}$, while SFCMO showed a pore volume of 0.018 $cm^3\,g^{-1}$. The results for both catalysts are displayed in Fig. 7. It should be noted that BET surface area employed for normalization of catalytic activity is determined *ex-situ* and may not fully reflect the active surface under high-temperature reaction conditions.

The results reinforce the superior catalytic properties of SFMO, due to the higher Specific Surface Activity (r), especially for temperatures in the range of 600–700 °C. The difference in the Specific Surface Activity between the two catalysts is likely related to their composition, particularly the concentration and oxidation state of each cation, as N_2O catalytic decomposition is reported to follow a redox mechanism involving coordinatively unsaturated surface cations [32]. In this context, modifying B-site composition of the perovskite may significantly alter the availability and reactivity of redox-active surface cations. As previously mentioned, Co substitution may influence the redox equilibrium of the transition metal cations in SFMO (*e.g.*, Fe^{3+}/Fe^{2+}) and promote the formation of oxygen vacancies as a charge-compensation mechanism, particularly at elevated temperatures. These defects can modify the redox behaviour and oxygen mobility, thereby affecting its catalytic performance [16,31]. Nonetheless, in the current work, the Co-containing perovskite is shown to exhibit a

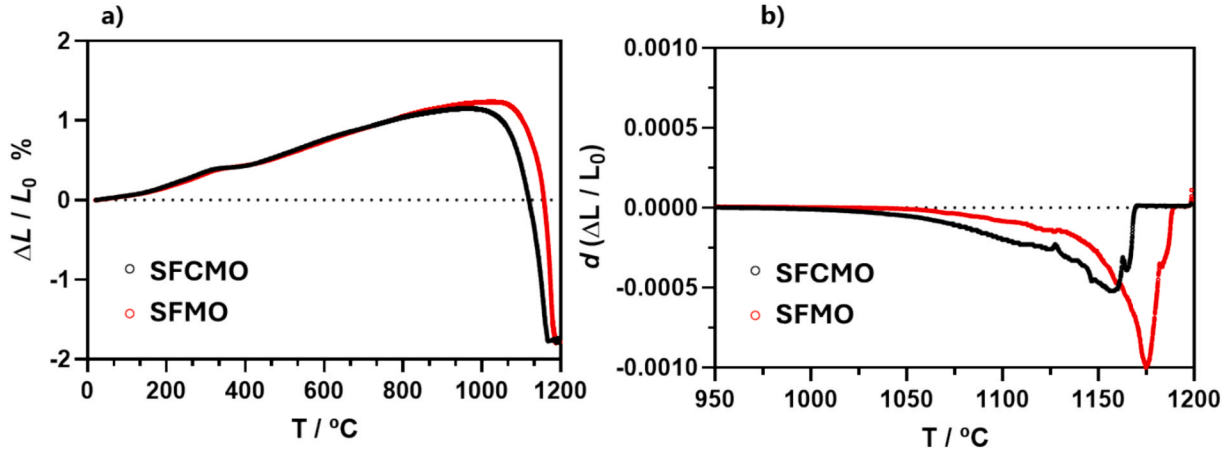

Fig. 5. (a) shrinkage curves obtained in the range of temperatures between 21 °C and 1200 °C for SFMO and SCMO and (b) their derivatives.

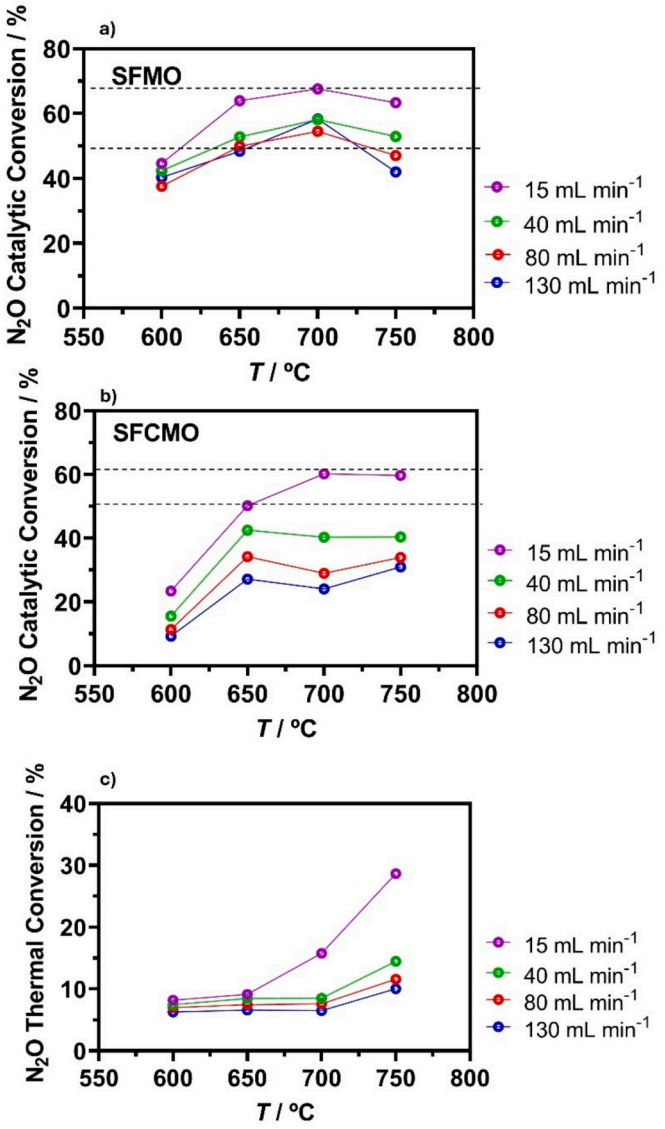

Fig. 6. N_2O conversion for the temperature range of 600 to 750 °C: (a) catalytic conversion of N_2O over SFMO and (b) the catalytic conversion of N_2O over SFCMO perovskite; (c) thermal conversion for N_2O gas flow rates of 15, 40, 80 and 130 mL min^{-1}, corresponding to GHSV of 4500, 12 000, 24 000, and 39 000 h^{-1}.

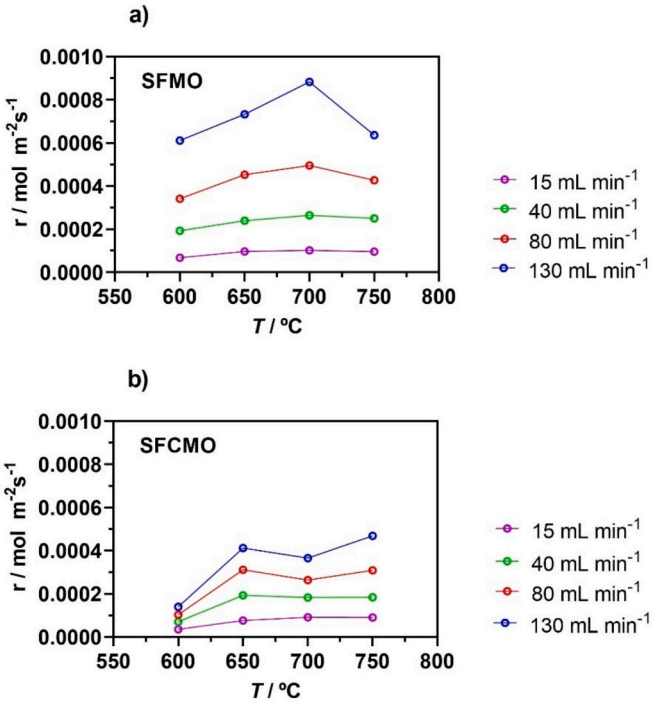

Fig. 7. Specific surface activity for (a) SFMO and (b) SFMO for the temperature range of 600 – 750 °C.

catalytic activity valley at 700 °C, with activity increasing slightly at lower and higher temperatures within the 650 °C to 750 °C range.

To shed light on this observation, XPS analyses were performed. Interestingly, the XPS results show no detectable Co^{2+}/ Co^{3+} species at the SFCMO surface – Fig. 8 (**b**), possibly due to the low level of Co-substitution in the SFCMO sample.

The examination of the Mo3d region of the XPS spectra – Fig. 8 (**a**) and (**c**)- revealed quite different surface characteristics between the two samples. In SFMO the presence of Mo was observed at the surface with different oxidation states, specifically Mo^{6+}, Mo^{5+} and Mo^{4+}, whereas only Mo^{6+} was found in the SFCMO (Fig. 8(**a**)).

The availability of multiple oxidation states of Mo observed in the SFMO sample may provide a basis for its higher catalytic activity by enhancing the surface electron-donating capability through access to Mo redox couples, thereby facilitating N_2O activation and N-O bond cleavage [33]. This behaviour may help explain the decrease in performance observed in the SFMO catalyst at 750 °C. At elevated temperatures,

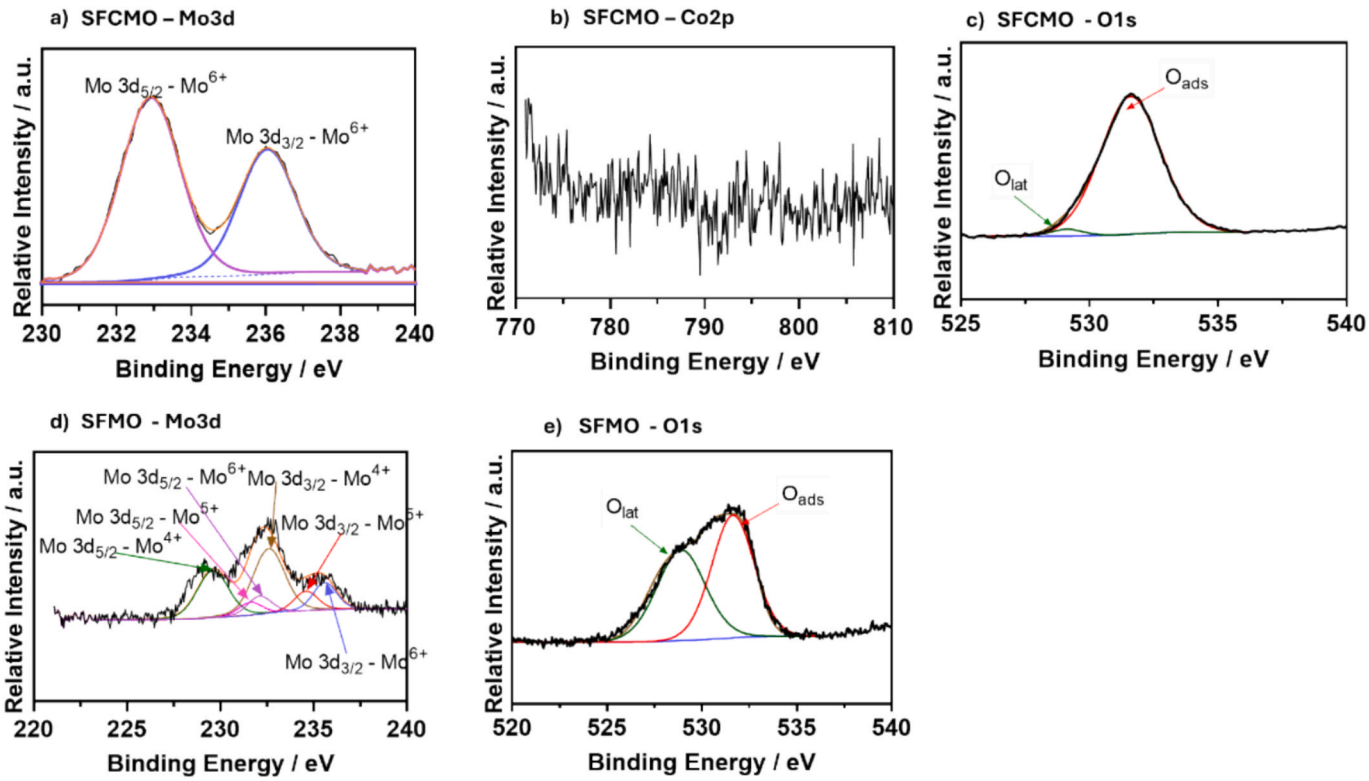

Fig. 8. XPS spectra for SFCMO at room temperature: (a) SFCMO, Mo3d region, (b) SFCMO, Co2p region, (c) SFCMO, O1s region, (d) SFMO, Mo3d region and (e) SFMO, O1s region.

molybdenum may progressively reduce to lower oxidation states, altering the redox balance of the catalyst and impairing its ability to sustain the efficient electron donation required for N-O bond cleavage. In contrast, XPS analysis of the Co-doped sample reveals that Mo remains predominantly in the Mo^{6+} state. This suggests that Co incorporation modifies the redox equilibrium within the lattice and may help stabilize Mo in its high oxidation state. Such stabilization could limit the availability of Mo redox couples participating in surface electron-transfer processes, which may be necessary for efficient N_2O activation and high catalytic activity [34]. However, the exact mechanism underlying this stabilization cannot be fully resolved based on the present *ex-situ* data and would require further investigation, namely based on operando techniques.

Consistent with this interpretation, minor non-monotonic variations in the N_2O conversion are observed for SFCMO at higher flow rates, with a slight dip around 700 °C followed by a recovery at 750 °C. The small magnitude of this variation likely reflects temperature-dependent surface redox adjustments – a transient reorganization of surface species within this temperature window – rather than a significant change in intrinsic catalytic properties. Thermogravimetric analysis (Fig. 4) indicates increased oxygen loss in the 600–800 °C range, suggesting progressive reduction of the oxide lattice. Such temperature-induced oxygen release may influence the redox state of transition-metal cations and modify surface reactivity. This effect could change oxygen removal during catalysis and may partially account for the improved catalytic response at 750 °C. Similar temperature-dependent oxygen mobility and surface redox processes have been reported to influence N_2O decomposition over perovskite catalysts [35]. Note that the examination of the O1s region from the XPS spectra for SFCMO shows a relatively higher O_{ads}/O_{lat} contribution in SFCMO compared to SFMO (Fig. 8 **(c)** and **(e)**), suggesting an increased presence of oxygen vacancy-related environments. It should be noted, however, that this comparison is based on relative peak contributions and remains qualitative, although, it is supported by TGA discussion.

Additionally, XPS analysis showed that Co is not significant at the surface of SFCMO catalyst, suggesting that mixed Co oxidation states do not directly contribute to surface redox activity. Instead, Co appears to primarily stabilise Mo in a higher oxidation state. The weak Co signal observed by XPS is consistent with the low doping level. Complementary *post-mortem* SEM-EDS analysis (in Section 3. 4) confirms the presence of Co within the electrode, suggesting that Co is homogeneously distributed across the electrode thickness. This observation supports the interpretation that Co primarily modifies the material's overall surface redox chemistry, while its limited presence reduces its direct involvement in catalytic processes. Consequently, Co is expected to play a significant role in the electrochemical behavior of the electrode, particularly through its expected influence on microstructure, as discussed in the following section.

3.3. Electrochemical characterization

3.3.1. Analysis under open circuit potential (OCP) conditions

Fig. 9 portrays the Nyquist plots obtained in the experiments performed using the MEAs comprising the SFMO (green spectra) and SFCMO (red spectra) perovskites (SFMO/SFCMO||CGO||YSZ||Ni-YSZ). These results were collected at 750 °C, under open-circuit potential (OCP) conditions, with N_2O fed to the cathode and NH_3 as the anode fuel. As the cells operate under the same conditions and differ only in the cathode, differences in performance should be primarily attributed to the cathode. Nevertheless, a minor contribution from the anode cannot be entirely excluded. Therefore, the present analysis focuses on the cathodic reaction.

The Nyquist plots for the cells SFMO and SFCMO demonstrate the existence of at least two limiting processes: one at high frequencies and another at intermediate frequencies. The SFCMO electrode shows an additional limiting process at low frequencies that is not observed in the SFMO one. Thus, two different equivalent circuit models (ECMs) were used to fit the experimental data: the equivalent circuit models

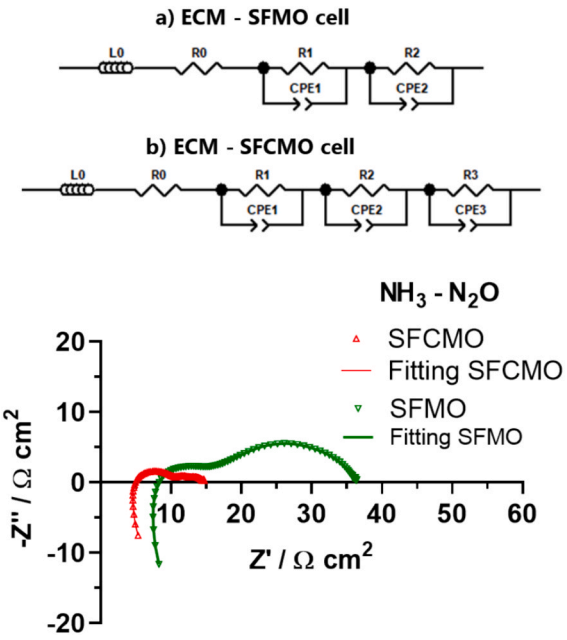

Fig. 9. Nyquist plots of the SFCMO/SFMO − CGO20/YSZ/NiO MEA measured at 750 °C under open circuit potential, fed with pure N_2O to the cathode and pure NH_3 to the anode. (a) and (b) show the equivalent electric circuits used to fit Nyquist plots of SFMO and SFCMO cells, respectively.

comprises an inductor (L_0), that results from the wiring and electrical connectors in the setup, a series resistance (R_0) (the ohmic contribution), followed by two and three $R||$CPE in series, arranged in parallel, for SFMO and SFCMO electrodes, respectively; the $R||$CPE elements represent a resistance in parallel to a constant phase element (CPE), which describes a semi-circle in the frequency domain [36]. The fitting curves are shown in Fig. 9 as continuous lines and provide a good fit to the experimental data. For each experiment, the total polarization resistance (R_p) was calculated by adding all the contributions ($R_p = R_1 + R_2 + R_3$), specifically the resistances at high (R_1), middle (R_2), and low (R_3) frequencies. The resultant information extracted from the fitting of the Nyquist plots to the models is presented in Table 2.

The ohmic resistance (R_0) differs between the two electrodes, where the SFMO cell presents a significantly higher ohmic resistance (Table 2), which was attributed to the interface resistance between the SFMO cathode layer and the CGO20 buffer layer. As can be seen in Fig. 10, the interface cathode-buffer layer – highlighted in red in Fig. 10 **(a)** and **(b)** – shows gaps in the case of SFMO electrode. The improved contact between layers, observed in the SFMO electrode, is expected to enhance ionic current collection at the electrode–electrolyte interface, given the larger effective contact area, reflected by a decrease in the ohmic losses (R_0) [37]. Furthermore, the enhanced microstructural connectivity and the consequent increase in the electroactive area contribute to lowering polarization resistance (R_p), consistent with the approximately threefold higher R_p of SFMO cell relative to SFCMO [38,39].

The $R_1||CPE_1$ equivalent circuit element observed in the high-frequency region of the Nyquist plot ($W_1 = 10^4$ Hz, Table 2), yields an effective capacitance of $\sim 10^{-7} - 10^{-6}$ F cm^{-2} (Table 2), and is related to an interfacial polarization phenomenon [37,40]. In this work, it could be related to the typical oxygen-ion transfer across the cathode (SFMO or SFCMO)-electrolyte (YSZ) interface, namely within CGO20 buffer layer [37,40] In this respect, this oxygen transfer is corroborated by the $\varnothing_1$ term, which describes the deviation from ideal capacitive behavior and is associated with the depression of the corresponding semicircle in Nyquist plot. For both samples, $\varnothing_1$ is close to 0.5 (Table 2), corroborating the diffusional nature of the $R_1||CPE_1$ contribution [41].

The lower R_1 value observed in the SFCMO sample compared to the SFMO, which is approximately half of that undoped electrode (Table 2), can be associated with the improved microstructural densification near the cathode-buffer layer interface, as evidenced by the more compact structure observed in Fig. 10 **(b)**. This increased densification enhances grain connectivity and increases the local solid volume fraction at the electrode–electrolyte interface relative to the more porous SFMO electrode structure (Fig. 10 **(a)**) [18]. A higher solid volume fraction in this interfacial region is known to enhance ambipolar conductivity by facilitating both ionic and electronic transport, particularly within the electrochemically active zone adjacent to the electrolyte [18]. This enhanced transport balance promotes more efficient oxygen reduction reaction, thereby contributing to the reduced polarization resistance observed for SFCMO cell [42–44].

In addition to microstructural effects, the partial substitution of Fe by Co may further enhance oxygen-ion transport properties. Co incorporation has been reported to increase oxygen vacancy concentration (corroborating the previous TGA discussion) and/or enhance oxygen ion conductivity due to modified metal–oxygen bonding characteristics (Co-O-Co bounds are weaker than Fe-O-Fe [15]), which could further accelerate oxygen ion transport kinetics [45]. However, although this contribution cannot be excluded, the microstructural improvement

Table 2
Fitting results for the Nyquist plots obtained at 750 °C and the calculated polarization resistances from the selected equivalent circuit models (ECMs); C, R, and W are the capacitance, resistance, and the relaxation frequency of each process, respectively. $\varnothing$ denotes the exponent of the Z_{CPE}, which is associated with the relaxation behaviour of the corresponding semi-circle and reflects the deviation from ideal capacitive behaviour.

Gas composition	**NH_3 (anode side) N_2O (cathode side)**	
Catalyst	**SFMO**	**SFCMO**
R_0 / Ω cm^2	7.02	4.92
R_1 / Ω cm^2	14.40	7.35
C_1 / F cm^{-2}	3.97×10^{-7}	2.12×10^{-6}
W_1 / Hz	2.81×10^{4}	1.02×10^{4}
$\varnothing_1$	0.39	0.53
R_2 / Ω cm^2	18.51	1.50
C_2 / F cm^{-2}	8.09×10^{-4}	5.10×10^{-3}
W_2 / Hz	1.06×10^{1}	2.08×10^{1}
$\varnothing_2$	0.65	0.84
R_3 / Ω cm^2		2.08
C_3 / F cm^{-2}		1.33×10^{-1}
W_3 / Hz		0.575
$\varnothing_3$		0.68
R_p / Ω cm^2	32.91	10.93

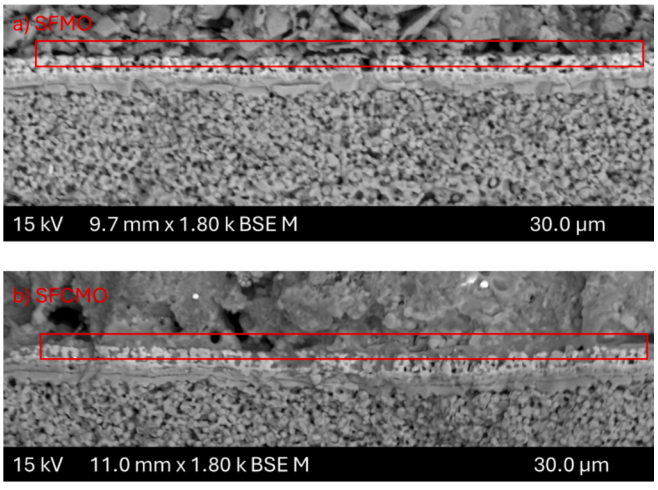

Fig. 10. SEM images of the membrane electrode assemblies containing (a) SFMO||CGO||YSZ||NiO and (b) SFCMO||CGO||YSZ||NiO.

appears to play a dominant role in the observed reduction in R_1.

The R_2 and C_{CPE2} characterise the RC equivalent circuit, corresponding to the intermediate-frequency region of the Nyquist plot ($W_2 = 10^1$ Hz, Table 2), displaying effective capacitances of ~ 10^{-4} and 10^{-3} F cm^{-2} (Table 2). Such values are typically associated with charge-transfer related to the ORR at the electrocatalyst surface and/or with solid-state oxygen diffusion, including both bulk and surface contributions [37].

A significant decrease in the polarization resistance in $R_2||CPE_2$ equivalent circuit element is noticed upon Co incorporation, with R_2 decreasing about 12 times (18.51 Ω cm^2 for SFMO *vs*. 1.50 Ω cm^2 for SFCMO, Table 2). This substantial reduction indicates that this process becomes significantly less limiting in the Co-doped electrode. Given that $R_2||CPE_2$ element has been associated with surface charge-transfer and/or with solid-state oxygen diffusion, this decrease was assigned to the enhanced grain-to-grain connectivity observed in SFCMO electrode microstructure. Improved solid-state connectivity can reduce tortuosity and enhance both ionic and electronic percolation pathways, particularly near the electrolyte interface, where oxygen ions are incorporated into the electrolyte. Such microstructural improvements have been reported to enhance ambipolar conductivity in MIEC cathodes [18], thereby facilitating oxygen-ion migration through continuous solid pathways. This effect can extend the electrochemically active region for ORR and contribute to the observed reduced polarization resistance [18,37].

Meanwhile, the low-frequency process ($R_3||CPE_3$ element) – 10^{-1} Hz) was only observed in the SFCMO cell with effective capacitance values in the range of 10^{-1}F cm^{-2}. In addition, the non-ideal behaviour reflected by $\varnothing_3$ value of 0.68 suggests a diffusional process occurring within a heterogeneous porous structure. The absence of this arc in the Nyquist plot of a cell containing the more porous SFMO electrode, together with the increase in the densification of the SFCMO cathode, supports the interpretation that this process may be associated with gas diffusion limitations.

Fig. 11 illustrates the temperature dependence of the total (R_p) and elementary polarization (R_1, R_2, and R_3) resistances obtained for both fuel cells, measured in the temperature interval of 600 – 750 °C, under OCP conditions; the E_a depicts the activation energy of each polarization resistance. It is observed that the E_a values obtained for R_p, R_1, and R_2 are essentially similar between samples for each process. The similarity suggests that the dominant kinetic process governing each polarization contribution remains unchanged upon Co doping, thus corroborating a similar electrode mechanism for both SFMO and SFCMO samples. Moreover, the low-temperature dependence of R_3 ($E_a = 0.16$ eV, Fig. 11) indicates a weak temperature dependence, which is consistent with gas diffusion as the rate-limiting step; this contribution is typically only distinguishable in the Nyquist plot at high temperatures when kinetic resistances decrease, and mass transport become comparatively more evident [46–48].

Across the investigated temperature range, all polarization resistance contributions are lower for the SFCMO, confirming the overall beneficial effect of cobalt incorporation. Interestingly, the dominant rate-limiting contribution differs between the two electrodes: R_1 governs the polarization behaviour in the SFCMO cell, whereas R_2 represents the primary limitation in the SFMO cell. In the SFCMO cell, R_1 is nearly one order of magnitude higher than R_2 (Fig. 11). In contrast, the SFMO cell exhibits the opposite trend, indicating a redistribution of the dominant polarization processes upon cobalt substitution.

The R_2 and C_{CPE2} values, which characterize the second semicircle of the Nyquist plot, have previously been attributed to either charge-transfer reactions occurring at the electrocatalyst surface and/or to the solid-state diffusion of oxygen species within the cathode [37]. The different behaviour observed between the samples suggests that the nature of this process depends on the cathode electrode's microstructure. In the SFMO-based cell, the lower packing density and reduced grain connectivity may hinder oxygen-ion transport through the solid network. In this case, the $R_2||CPE_2$ element contribution is likely partially governed by solid-state oxygen diffusion. This interpretation is supported by the $\varnothing_2$ value of 0.65 (Table 2), which indicates a significant diffusional character [41]. Conversely, the increased densification and improved grain-to-grain contact in the SFCMO electrode likely promote more efficient solid-state oxygen transport [38]. As diffusion becomes a less limiting process, the $R_2||CPE_2$ element contribution may shift to the control of charge-transfer reactions at the electrocatalyst surface. The higher $\varnothing_2$ value (0.84, Table 2) further supports a more capacitive behavior, typically associated with surface-controlled processes.

3.3.2. *Analysis under applied polarization conditions*

Fig. 12 shows the electrode polarization resistance as a function of the applied potential difference (ΔV) at 750 °C under N_2O atmosphere at the cathode and NH_3 at the anode for both cells. In the case of the SFMO cell (Fig. 12 **a**), the total polarization resistance (R_p) and the elementary polarization resistances (R_1, R_2, and R_3) consistently decrease with increasing potential difference (ΔV). This is due to an increase in the driving force for the electrochemical reactions [49]. However, a different trend is observed in the SFCMO electrode, where an initial increase in resistance is observed in almost all resistive components, reaching a peak at @ −0.2 V, after which it begins to decrease until −1 V – Fig. 12 (**b**).

This behaviour was assigned to a transient mismatch between electrode bulk oxygen-ion transport and surface exchange process kinetics under mild polarization [50]. Under these conditions, the rate of vacancy transport through the electrode and electrolyte may exceed the rate of oxygen incorporation at the surface, leading to a temporary limitation in the surface exchange process [50]. The denser microstructure of SFCMO could further reduce the effective available surface area for oxygen exchange, thereby amplifying this effect. Similar trends have been reported by different studies [13,51]. On the other hand, as

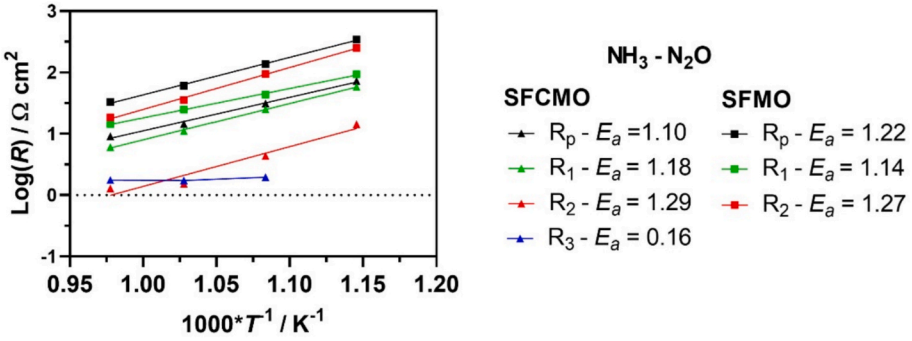

Fig. 11. The temperature dependence of total (R_p), high-frequency (R_1) and, intermediate-frequency (R_2), and low-frequency (R_3) polarisation resistances at open circuit potential for SFMO (triangle symbol) and SFCMO cells (square symbol), operating under N_2O as oxidant and a) NH_3 as fuel, for operation temperature between 600 °C and 750 °C.

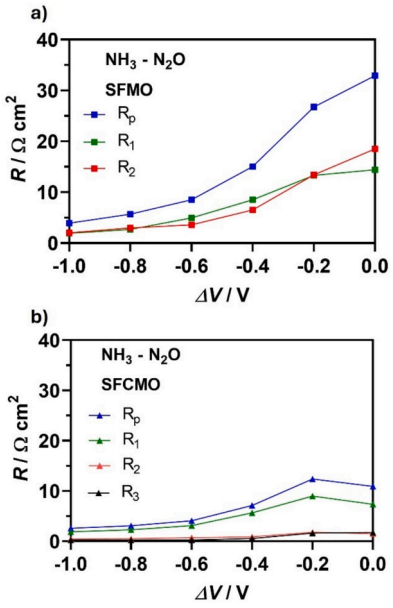

Fig. 12. Dependence of the applied difference of potential on (a) SFMO (square symbol) and (b) SFCMO cell (triangle symbol), at 750 °C, in the total (R_p), high-frequency (R_1), and middle-frequency (R_2) polarisation resistances under N_2O at the cathode and fueling anode with NH_3.

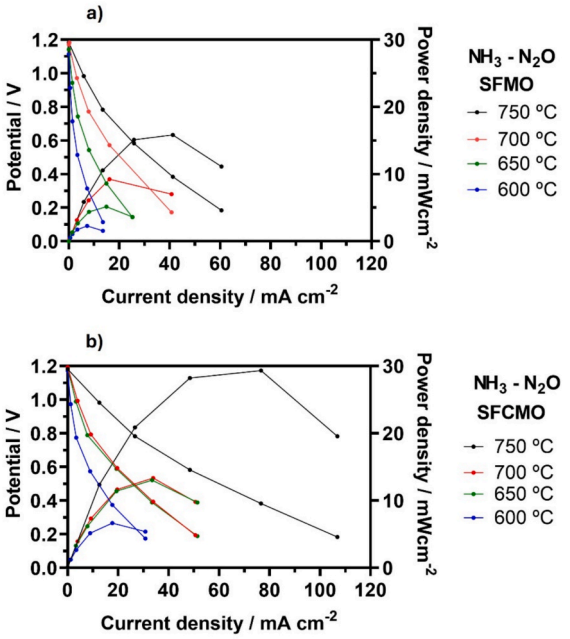

Fig. 13. Current-potential difference (*I-V*) characteristics of each cell – a) SFMO and b) SFCMO – performed in the temperature range of 750—600 °C, under N_2O at the cathode and fueling anode with NH_3.

ΔV increases, both surface exchange and solid-state oxygen diffusion rates are significantly enhanced, ultimately reducing the polarization resistance.

Overall, the SFCMO cell performs better under polarization than SFMO. This improvement is likely related to its denser microstructure, which reduces transport-related limitations within the cathode and lowers polarization resistance, thereby improving oxygen reduction reaction kinetics under polarization, despite the slightly lower intrinsic catalytic activity of this material.

3.3.3. *I-V characteristic curves*

This section evaluates the performance of each cell (SFMO/SFCMO||CGO-20||YSZ||NiO MEA) for the simultaneous electrochemical reduction of N_2O and electrochemical oxidation of NH_3. Each cell was tested over the temperature range of 600–750 °C, with 50 mL min^{-1} of N_2O fed to the cathode and 50 mL min^{-1} of NH_3 fed to the anode. The current–voltage difference (*I-V*) characteristics and the corresponding power density curves for each cell are presented in Fig. 13.

The effect of temperature is evident in both cells: higher operating temperatures favor higher power output, consistent with the thermally activated nature of the membrane electrode assembly composing materials. The highest peak power density was obtained for the cell incorporating the Co-doped perovskite, reaching nearly 30 mW cm^{-2}. This value decreases by approximately 33 %, 35 %, and 50 % as the operating temperature is reduced from 700 °C to 650 °C and to 600 °C.

The SFMO cell exhibits a similar trend, but with notably lower performance. Its maximum power density is approximately half that of the SFCMO cell (~16 mW cm^{-2}), and the power density decreases by about 43 %, 44 %, and 54 % as the operating temperature is reduced from 700 °C to 650 °C and to 600 °C, respectively.

Moreover, the OCP values recorded for the SFCMO cell are consistently higher across the investigated temperature range (Table 3), further indicating the superior electrocatalytic behavior of the SFCMO electrode toward N_2O decomposition.

The OCP values for both SFMO and SFCMO decrease with decreasing temperature, in agreement with the expected Nernstian behaviour. A slightly more pronounced drop is observed at 600 °C, particularly for SFMO. This deviation is likely an artifact related to minor experimental factors, such as small variations in sealing tightness, which can become more pronounced at lower temperatures and after multiple experimental trials. Importantly, the overall trend and comparison between materials remain consistent.

Table 3
Open circuit potential (OCP) values obtained for the SFMO and SFCMO MEA for the operating temperatures in the range of 750–600 °C.

T / °C	OCP	
	SFMO	SFCMO
750	1.18	1.18
700	1.18	1.19
650	1.14	1.19
600	1.11	1.17

It should be noted that state-of-the-art SOFCs operating with hydrogen can achieve peak power densities of *ca.* 1 W cm^{-2} [52]. However, these systems are highly optimized and operate under conventional conditions. For DA-SOFC, peak power densities of approximately 60–100 mW cm^{-2} at 750–800 °C have been reported using Ni-YSZ as anode material [53,54], which are of same order of magnitude as the results obtained in the present work. Higher performances (~700 mW cm^{-2} at 850 °C) have also been reported for better-optimized systems [55], although these systems typically operate under standard oxidizing atmospheres (air or O_2). More relevant, a recent work reports a SOFC operating on N_2O at the cathode, achieving power densities of *ca.* 200 W cm^{-2} at 650 °C using a dual-phase $La_{0.6}Sr_{0.4}Co_{0.2}Fe_{0.8}O_{3-\delta}$ – $Gd_{0.1}Ce_{0.9}O_{2-\delta}$ (LSCF-GDC) cathode [3]. However, this system used hydrogen as the fuel, thereby avoiding the additional reaction step associated with ammonia decomposition and therefore offering a simpler fuel system.

In contrast, the present work investigates a more complex and less studied configuration, combining N_2O-containing atmospheres with NH_3 as the fuel. Under these conditions, the cathodic reaction involves N_2O reduction rather than the conventional oxygen reduction reaction, introducing kinetic limitations and fundamentally different reaction pathways. Consequently, direct comparison with conventional or previously reported DA-SOFCs systems is not straightforward. Within this

context, the achieved performance (~30 mW cm^{-2} at 750 °C) is considered very promising and, more importantly, demonstrates a clear improvement compared to the undoped SFMO, highlighting the effectiveness of the Co-doping strategy.

The distinctive electrochemical behaviour of SFCMO electrode highlights its effectiveness as cathode material for operation under N_2O – containing atmospheres in DA-SOFC systems. In particular, the superior performance of SFCMO can be attributed to its enhanced microstructural features, including improved grain connectivity and more favorable electrode architecture, which facilitate charge transport and increase the effective electrochemical active area. These characteristics contribute to reduced polarization resistance and, consequently, to higher power density. In contrast, SFMO exhibits concentration of reduced Mo^{4+} species, which promotes surface-driven catalytic activity but results in more heterogeneous bulk transport properties. As a result, SFCMO demonstrated more stable electrochemical behaviour, whereas SFMO exhibits superior intrinsic catalytic activity, in good agreement with the XPS analysis. Therefore, although SFMO provides higher intrinsic catalytic activity for N_2O reduction – likely due to the greater availability of redox-active pairs – its comparatively less optimized microstructure limits its overall electrochemical efficiency under operating conditions.

3.4. Post-mortem analysis

To assess possible morphological changing in the electrodes during electrochemical tests, both cells were analyzed by scanning electron microscopy (SEM). Fig. 14 **(a)** and **(b)** show cross-sectional views of the SFMO and SFCMO MEAs, respectively, after operation. In both cases, the different layers are clearly distinguished: (a) the cathode layer composed of the synthesized electrode layer (SFMO or SFCMO), (b) the CGO20 buffer layer, and (c) the YSZ electrolyte layer.

Both electrodes show no chemical reactivity between the cathode and the electrolyte/buffer layer, specifically strontium diffusion to these adjacent layers, as depicted in the *post-mortem* energy dispersive spectroscopy (EDS) images of the MEA cross-section for SFMO and SFCMO cells, in Fig. 15. This avoids the formation of strontium zirconate, which increases resistance and reduces the overall efficiency of the SOFC [56,57]. This was only possible due to the stability of the CGO and YSZ layers under the applied sintering temperature (1000 °C).

Fig. 16 depicts the Nyquist plots obtained under OCP conditions, before each experiment and after polarization studies, for the temperatures between 600–750 °C, under N_2O in the cathode and using NH_3 in the anode. Fig. 16 **(a)** shows the results for the cell composed by SFMO and Fig. 16 **(b)** shows the results for the cell composed by SFCMO.

These Nyquist plots, for both cells, show similar behaviors before and after polarization, at each studied temperature, indicative of almost no degradation of the cells due to operating conditions.

4. Conclusions

This work aimed to enhance the performance of SFMO electrode by incorporating Co into its structure and to elucidate the role of Co in the direct-ammonia solid oxide fuel cell (DA-SOFC) for N_2O abatement operating at intermediate temperatures (600–750 °C).

Partial substitution at the B-site of $Sr_2Fe_{1.5}Mo_{0.5}O_{6-\delta}$ with a small amount of cobalt ($x = 0.05$) proved an effective strategy for microstructural optimization, eliminating the need for high sintering temperatures and promoting improved grain connectivity. The denser microstructure resulted in an approximately threefold reduction in polarization resistance, thereby enhancing electronic transport and overall cathode performance. Moreover, Co incorporation had a positive impact on intrinsic properties, as evidenced by a slight increase in oxygen non-stoichiometry ($\Delta\delta$ from 0.50 to 0.55 @ 1000 °C for SFMO and SFCMO, respectively), along with improved electrical properties reflected in reduced polarization resistance. Conversely, Co addition did not increase catalytic activity, most likely because it increased the Mo oxidation state, thereby compensating for the charge.

Electrochemical impedance spectroscopy responses, particularly in the intermediate-frequency region, related to the surface exchange process kinetics and the solid-state diffusion of O^{2-}, revealed similar ORR mechanisms for both cells, also consistent with the comparable activation energies determined. Some differences, however, were assigned to differences in electrode microstructure. In this regard, the SFCMO cell exhibited markedly superior electrochemical performance. The maximum power density of the cell containing the Co-doped cathode was nearly twice that of the undoped SFMO, reaching approximately 30 mW cm^{-2}. Overall, the improved SFMO performance through Co doping can be attributed in part to a slightly higher concentration of oxygen-ion vacancies, but predominantly to microstructural optimization. These findings demonstrate that low-level Co doping is a simple yet effective strategy to enhance electrical properties through microstructure control. This approach provides valuable insights for designing higher-performance SFMO cathodes and significantly improving the electrochemical activity for practical SOFC applications under low oxygen partial pressure conditions, without increasing electrode sintering temperatures, which are typically constrained by component interactions.

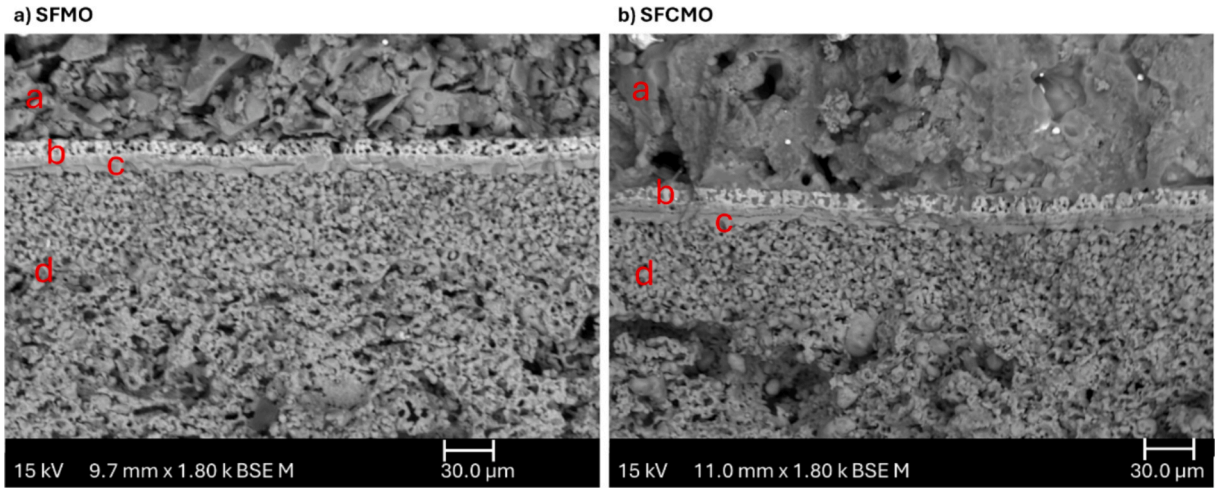

Fig. 14. Scanning electron microscopy images (SEM) of cross-section microstructure of the MEA: a: cathode – SFCMO, b: buffer layer – CGO, c: electrolyte – YSZ, and d: anode – Ni-YSZ.

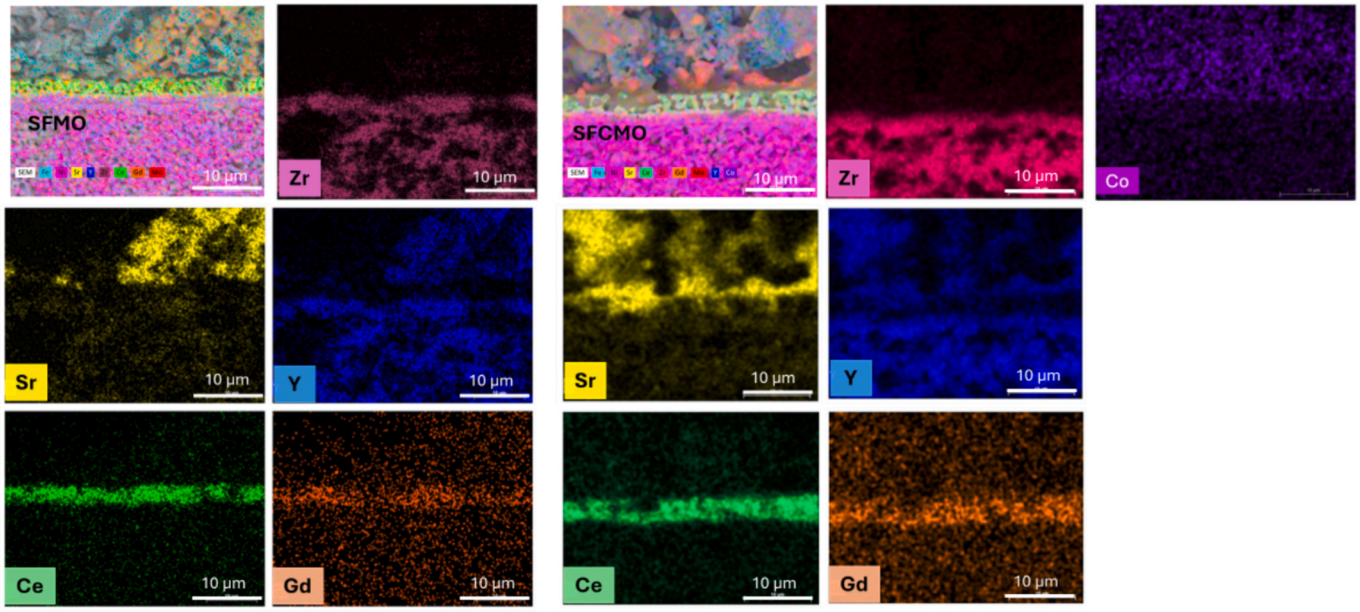

Fig. 15. EDS mapping images of cross-section microstructure of the SFMO and SFCMO MEA, showing the cathode, buffer layer- CGO and electrolyte –YSZ, with no Sr diffusion across these layers.

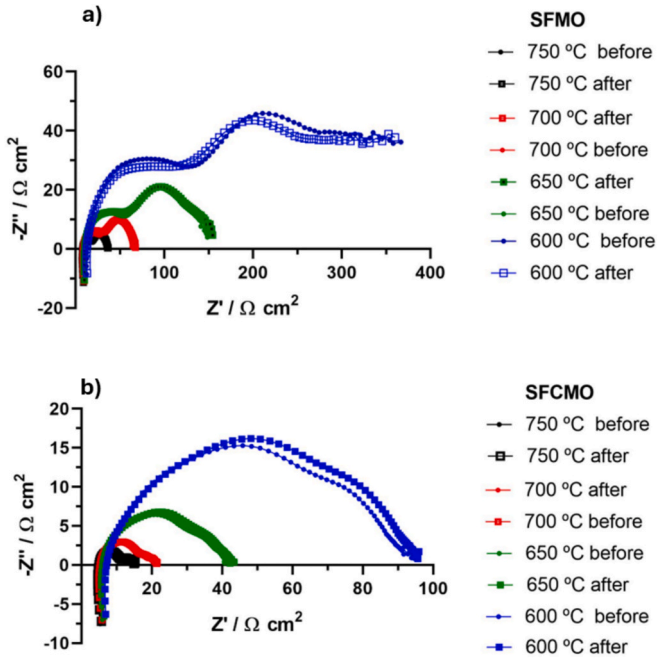

Fig. 16. Nyquist plots of the a) SFMO b) SFCMO – CGO20/YSZ/NiO MEA measured at 750 °C under OCP feeding N_2O to the cathode and NH_3 to the anode.

CRediT authorship contribution statement

Celina Fernandes: Writing – original draft, Methodology, Investigation, Formal analysis, Data curation, Conceptualization. **Laura I.V. Holz:** . **Francisco J.A. Loureiro:** . **Sergey M. Mikhalev:** Investigation, Formal analysis. **Duncan P. Fagg:** . **Adélio Mendes:** Writing – review & editing, Supervision, Resources, Project administration, Funding acquisition.

Declaration of competing interest

The authors declare that they have no known competing financial interests or personal relationships that could have appeared to influence the work reported in this paper.

Acknowledgments

This work was supported by national funds through FCT/MECI: LEPABE, UID/00511/2025 (https://doi.org/10.54499/UID/00511/2025) and UID/PRR/00511/2025 (https://doi.org/10.54499/UID/PRR/00511/2025) and ALiCE, LA/P/0045/2020 (https://doi.org/10.54499/LA/P/0045/2020). This work is a result of project HI_MOV – "Corredor Tecnológico Transfronterizo de Movilidad com Hidrógeno Renovable", with reference 0160_HI_MOV_1_E, cofinanced by European Regional Development Fund (ERDF), through Programa de Cooperação INTERREG VI A Espanha – Portugal (POCTEP) 2021-2027. The authors also acknowledge the following projects: 2022.02498.PTDC (https://doi.org/10.54499/2022.02498.PTDC), 2022.09319.PTDC (https://doi.org/10.54499/2022.09319.PTDC), UIDB/00481/2020 (https://doi.org/10.54499/UIDB/00481/2020), and UIDP/00481/2020 (https://doi.org/10.54499/UIDP/00481/2020) from Fundação para a Ciência e Tecnologia (FCT); and CENTRO-01-0145-FEDER-022083 from Centro Portugal Regional Operational Programme (Centro2020), under the PORTUGAL 2020 Partnership Agreement, through the European Regional Development Fund (ERDF). Celina Fernandes, Laura Holz and Francisco Loureiro acknowledge FCT for the PhD and CEEC grants (2021.07014.BD), 2023.05868.CEECIND/CP2840/CT0021 (https://doi.org/10.54499/2023.05868.CEECIND/CP2840/CT0021), 2020.02797.CEECIND/CP1589/CT0030 (https://doi.org/10.54499/2020.02797.CEECIND/CP1589/CT0030), respectively).

Data availability

Data will be made available on request.

References

[1] Tian H, et al. Global methane and nitrous oxide emissions from terrestrial ecosystems due to multiple environmental changes. Ecosyst Health Sustainability 2015;1(1):1–20. https://doi.org/10.1890/EHS14-0015.1.

[2] Alves L, et al. A comprehensive review of NOx and N2O mitigation from industrial streams. Renew Sustain Energy Rev 2022;155:111916. https://doi.org/10.1016/j.rser.2021.111916.

[3] Rong Y-T, et al. Efficient power generation in a solid oxide fuel cell using N2O as the oxidant. Rare Met 2025;44(8):5859–67. https://doi.org/10.1007/s12598-025-03305-y.

[4] Tsipis EV, Kharton VV. Electrode materials and reaction mechanisms in solid oxide fuel cells: a brief review : I Performance-determining factors. J Solid State Electrochem 2008;12(9):1039–60. https://doi.org/10.1007/s10008-007-0468-0.

[5] Dong F, et al. Achieving exceptional activity and durability toward oxygen reduction based on a cobalt-free perovskite for solid oxide fuel cells. Journal of Energy Chemistry 2021;62:653–9. https://doi.org/10.1016/j.jechem.2021.04.020.

[6] Cheng Q, Muhammad A, Kaario O, Ahmad Z, Martti L. Ammonia as a sustainable fuel: review and novel strategies. Renew Sustain Energy Rev 2025;207:114995. https://doi.org/10.1016/j.rser.2024.114995.

[7] Fernandes C, Holz LIV, Loureiro FJA, Duarte M, Fagg DP, Mendes A. Nitrous oxide abatement and valorization in an ammonia-fueled SOFC stack – Nitric oxide and electricity production. Chem Eng J 2024;502:157921. https://doi.org/10.1016/j.cej.2024.157921.

[8] S. Zarabi Golkhatmi, M. I. Asghar, and P. D. Lund, "A review on solid oxide fuel cell durability: Latest progress, mechanisms, and study tools," *Renewable and Sustainable Energy Reviews*, vol. 161, p. 112339, Jun. 2022, doi: 10.1016/j.rser.2022.112339.

[9] M. Bhavisha *et al.*, "Molybdenum Incorporated Strontium-Iron and Strontium-Cobalt ($SrBMoO_{3-\delta}$; B=Fe & Co) Perovskites: Preparation and Their Application on Oxidation of *Iso* -Eugenol into Vanillin," *Eur. J. Inorg. Chem.*, vol. 26, no. 3, Jan. 2023, doi: 10.1002/ejic.202200590.

[10] Liu Q, Yang C, Dong X, Chen F. Perovskite Sr2Fe1.5Mo0.5O6−δ as electrode materials for symmetrical solid oxide electrolysis cells. Int J Hydrogen Energy 2010;35(19):10039–44. https://doi.org/10.1016/j.ijhydene.2010.08.016.

[11] Suchaneck G, Artiukh E. Nonstoichiometric Strontium Ferromolybdate as an Electrode Material for Solid Oxide fuel Cells. Inorganics (Basel) Nov. 2022;10(12):230. https://doi.org/10.3390/inorganics10120230.

[12] Holz LIV, et al. Strontium iron molybdenum oxide as electrocatalyst for nitrous oxide reduction in solid oxide fuel cells. Int J Hydrogen Energy Feb. 2024;54:25–36. https://doi.org/10.1016/j.ijhydene.2023.05.251.

[13] Zapata-Ramírez V, Mather GC, Pérez-Coll D. Enhancement of electrochemical performance of SrFe0.5Co0.5O3-δ as air electrode for intermediate temperature solid oxide cells via Sb and Mo doping. Ceram Int Nov. 2023;49(22):36467–77. https://doi.org/10.1016/j.ceramint.2023.08.330.

[14] Santos JRD, et al. Understanding the cathodic polarisation behaviour of the misfit [Ca2CoO3−δ]q[CoO2] (C349) as oxygen electrode for IT-SOFC. Electrochim Acta Sep. 2018;285:214–20. https://doi.org/10.1016/j.electacta.2018.08.018.

[15] Pan X, Wang Z, He B, Wang S, Wu X, Xia C. Effect of Co doping on the electrochemical properties of Sr2Fe1.5Mo0.5O6 electrode for solid oxide fuel cell. Int J Hydrogen Energy Apr. 2013;38(10):4108–15. https://doi.org/10.1016/j.ijhydene.2013.01.121.

[16] Richards N, et al. Effect of the Preparation Method of LaSrCoFeOx Perovskites on the activity of N2O Decomposition. Catal Letters Jan. 2022;152(1):213–26. https://doi.org/10.1007/s10562-021-03619-3.

[17] Song J, Zhu T, Chen X, Ni W, Zhong Q. Cobalt and Titanium substituted SrFeO3 based perovskite as efficient symmetrical electrode for solid oxide fuel cell. J Materiomics Jun. 2020;6(2):377–84. https://doi.org/10.1016/j.jmat.2020.02.009.

[18] Araújo AJM, et al. Composite of calcium cobaltite with praseodymium-doped ceria: a promising new oxygen electrode for solid oxide cells. Int J Hydrogen Energy Aug. 2021;46(55):28258–69. https://doi.org/10.1016/j.ijhydene.2021.06.049.

[19] dos Santos-Gómez L, León-Reina L, Porras-Vázquez JM, Losilla ER, Marrero-López D. Chemical stability and compatibility of double perovskite anode materials for SOFCs. Solid State Ion May 2013;239:1–7. https://doi.org/10.1016/j.ssi.2013.03.005.

[20] Farzin YA, Babaei A, Skafte TL, Stamate E, Ataie A, Jensen SH. Low-temperature preparation and investigation of electrochemical properties of SFM/CGO composite electrode. Solid State Ion Nov. 2020;356:115435. https://doi.org/10.1016/j.ssi.2020.115435.

[21] dos Santos-Gómez L, Hurtado J, Porras-Vázquez JM, Losilla ER, Marrero-López D. Durability and performance of CGO barriers and LSCF cathode deposited by spray-pyrolysis. J Eur Ceram Soc Aug. 2018;38(10):3518–26. https://doi.org/10.1016/j.jeurceramsoc.2018.03.024.

[22] Xu H, Cheng K, Chen M, Zhang L, Brodersen K, Du Y. Interdiffusion between gadolinia doped ceria and yttria stabilized zirconia in solid oxide fuel cells: Experimental investigation and kinetic modeling. J Power Sources Nov. 2019;441:227152. https://doi.org/10.1016/j.jpowsour.2019.227152.

[23] Fagg DP, García-Martin S, Kharton VV, Frade JR. Transport Properties of Fluorite-Type $Ce_{0.8}Pr_{0.2}O_{2-\delta}$: Optimization via the use of Cobalt Oxide Sintering Aid. Chem Mater Jan. 2009;21(2):381–91. https://doi.org/10.1021/cm802708a.

[24] Gu Y, et al. A brief review of high-entropy oxides in solid oxide fuel cell applications. Mater Sci Eng B May 2026;327:119260. https://doi.org/10.1016/j.mseb.2026.119260.

[25] Atomistic Simulation Group, "Data base of Ionic radii." Accessed: Jun. 03, 2025. [Online]. Available: http://abulafia.mt.ic.ac.uk/shannon/ptable.php.

[26] Zhou L, et al. Theoretical Investigation of the Oxygen Interaction on Co-doped YFeO3-δ as a Novel Cathode for Solid Oxide fuel Cells. Electrocatalysis Mar. 2022;13(2):165–74. https://doi.org/10.1007/s12678-022-00713-x.

[27] Stanley P, Hussain AM, Huang Y-L, Gritton JE, Wachsman ED. Defect chemistry and oxygen non-stoichiometry in SrFe0.2Co0.4Mo0.4O3-δ ceramic oxide for solid oxide fuel cells. Ionics (Kiel) Nov. 2020;26(11):5641–9. https://doi.org/10.1007/s11581-020-03674-7.

[28] Serrano-Lotina A, Mastronardo E, Coronado JM. Assessing the role of oxygen vacancies on N2O catalytic decomposition over CaMn1-xFexO3-δ perovskites. Appl Catal A Jan. 2025;689:120026. https://doi.org/10.1016/j.apcata.2024.120026.

[29] Konsolakis M. Recent advances on Nitrous Oxide (N_2O) Decomposition over Non-Noble-Metal Oxide Catalysts: Catalytic Performance, Mechanistic Considerations, and Surface Chemistry Aspects. ACS Catal Nov. 2015;5(11):6397–421. https://doi.org/10.1021/acscatal.5b01605.

[30] Richards N, et al. Lowering the Operating Temperature of Perovskite Catalysts for N_2O Decomposition through Control of Preparation Methods. ACS Catal May 2020;10(10):5430–42. https://doi.org/10.1021/acscatal.0c00698.

[31] Russo N, Mescia D, Fino D, Saracco G, Specchia V. N 2 O Decomposition over Perovskite Catalysts. Ind Eng Chem Res Jun. 2007;46(12):4226–31. https://doi.org/10.1021/ie0612008.

[32] Margellou AG, Vaimakis TC, Pomonis PJ, Petrakis DE. Catalytic N2O decomposition over La(Sr)FeO3 perovskites. React Kinet Mech Catal Aug. 2019;127(2):825–38. https://doi.org/10.1007/s11144-019-01608-7.

[33] Drago RS, Jurczyk K, Kob N. Catalyzed decomposition of N2O on metal oxide supports. Appl Catal B Sep. 1997;13(1):69–79. https://doi.org/10.1016/S0926-3373(96)00088-4.

[34] Chang H, García-Hernández M, Retuerto M, Alonso JA. Co-doped Sr2FeMoO6 double perovskites: a plausible scenario for phase segregation. Phys Rev B Mar. 2006;73(10):104417. https://doi.org/10.1103/PhysRevB.73.104417.

[35] Wu Y, Ni X, Beaurain A, Dujardin C, Granger P. Stoichiometric and non-stoichiometric perovskite-based catalysts: Consequences on surface properties and on catalytic performances in the decomposition of N2O from nitric acid plants. Appl Catal B 2012;125:149–57. https://doi.org/10.1016/j.apcatb.2012.05.033.

[36] Ch A, Lazanas, Prodromidis MI. Electrochemical Impedance Spectroscopy—A Tutorial. ACS Measurement Science Au Jun. 2023;3(3):162–93. https://doi.org/10.1021/acsmeasuresciau.2c00070.

[37] Park JH, Im H-N, Lee KT. Understanding redox cycling behavior of Ni–YSZ anodes at 500 °C in solid oxide fuel cells by electrochemical impedance analysis. J Korean Ceram Soc Sep. 2021;58(5):606–13. https://doi.org/10.1007/s43207-021-00136-2.

[38] Araújo AJM, et al. Optimization of misfit calcium cobaltite oxygen electrodes for solid oxide fuel cells through electrospinning processing. J Mater Chem A Mater 2024;12(38):26266–79. https://doi.org/10.1039/D4TA04085F.

[39] Melo KPV, Araújo AJM, Grilo JPF, Fagg DP, Macedo DA, Loureiro FJA. Understanding the oxygen reduction reaction of one-dimensional Ca3Co2O6 cathodes for SOFC. Int J Hydrogen Energy Feb. 2024;54:107–17. https://doi.org/10.1016/j.ijhydene.2023.05.186.

[40] Araújo AJM, et al. Creating new surface-exchange pathways on the misfit Ca-cobaltite electrode by the addition of an active interlayer. J Power Sources Oct. 2021;510:230417. https://doi.org/10.1016/j.jpowsour.2021.230417.

[41] Boukamp BA, Rolle A. Analysis and Application of distribution of Relaxation Times in Solid State Ionics. Solid State Ion Apr. 2017;302:12–8. https://doi.org/10.1016/j.ssi.2016.10.009.

[42] He A, Onishi J, Gong J, Shikazono N. Microstructure optimization of porous mixed ionic and electronic conducting cathode for solid oxide fuel cells. J Power Sources Dec. 2020;478:228771. https://doi.org/10.1016/j.jpowsour.2020.228771.

[43] Kim YT, Shikazono N. Evaluation of electrochemical reaction mechanisms of La0.6Sr0.4CoO3-δ-Gd0.1Ce0.9O2-δ composite cathodes by 3D numerical simulation. Solid State Ion Jun. 2018;319:162–9. https://doi.org/10.1016/j.ssi.2018.02.014.

[44] Zapata-Ramírez V, dos Santos-Gómez L, Mather GC, Marrero-López D, Pérez-Coll D. Enhanced Intermediate-Temperature Electrochemical Performance of Air Electrodes for Solid Oxide Cells with Spray-Pyrolyzed active Layers. ACS Appl Mater Interfaces Mar. 2020;12(9):10571–8. https://doi.org/10.1021/acsami.9b22966.

[45] Jørgensen MJ, Mogensen M. Impedance of Solid Oxide fuel Cell LSM/YSZ Composite Cathodes. J Electrochem Soc 2001;148(5):A433. https://doi.org/10.1149/1.1360203.

[46] Murray EP, Tsai T, Barnett SA. Oxygen transfer processes in (La,Sr)MnO3/Y2O3-stabilized ZrO2 cathodes: an impedance spectroscopy study. Solid State Ion Jul. 1998;110(3–4):235–43. https://doi.org/10.1016/S0167-2738(98)00142-8.

[47] Zapata-Ramírez V, Mather GC, Pérez-Coll D. Optimisation of electrochemical performance of Sr(Fe,Sb)O3-δ air electrodes for intermediate-temperature solid oxide cells through spray-pyrolysis processing. J Power Sources Apr. 2024;600:234243. https://doi.org/10.1016/j.jpowsour.2024.234243.

[48] Yoon SP, et al. Performance of anode-supported solid oxide fuel cell with La0.85Sr0.15MnO3 cathode modified by sol–gel coating technique. J Power Sources Apr. 2002;106(1–2):160–6. https://doi.org/10.1016/S0378-7753(01)01037-0.

[49] Boettcher SW, et al. Potentially Confusing: Potentials in Electrochemistry. ACS Energy Lett Jan. 2021;6(1):261–6. https://doi.org/10.1021/acsenergylett.0c02443.

[50] Pérez-Coll D, Aguadero A, Escudero MJ, Daza L. Effect of DC current polarization on the electrochemical behaviour of La2NiO4+δ and La3Ni2O7+δ-based systems. J Power Sources Jul. 2009;192(1):2–13. https://doi.org/10.1016/j.jpowsour.2008.10.073.

[51] Loureiro FJA, Araújo AJM, Paskocimas CA, Macedo DA, Fagg DP. Polarisation mechanism of the misfit Ca-cobaltite electrode for reversible solid oxide cells. Electrochim Acta Mar. 2021;373:137928. https://doi.org/10.1016/j.electacta.2021.137928.

[52] E. D. Wachsman and K. T. Lee, "Lowering the Temperature of Solid Oxide Fuel Cells," *Science (1979).*, vol. 334, no. 6058, pp. 935–939, Nov. 2011, doi: 10.1126/science.1204090.

[53] Elmutasim O, Dhawale DS, Giddey S, Paul G, Bhattacharya S. Unravelling the reaction mechanism on Ni–YSZ anode supported direct ammonia solid fuel cell: Experimental and theoretical studies. Appl Surf Sci Mar. 2025;686:162175. https://doi.org/10.1016/j.apsusc.2024.162175.

[54] Fournier GGM, Cumming IW, Hellgardt K. High performance direct ammonia solid oxide fuel cell. J Power Sources Nov. 2006;162(1):198–206. https://doi.org/10.1016/j.jpowsour.2006.06.047.

[55] Hagen A, Langnickel H, Sun X. Operation of solid oxide fuel cells with alternative hydrogen carriers. Int J Hydrogen Energy Jul. 2019;44(33):18382–92. https://doi.org/10.1016/j.ijhydene.2019.05.065.

[56] Lee S, Lee K, Lee J, Lee J, Kim T, Bae J. Evaluation of Electrolyte Materials of Gd- and Ce-Doped Scandia-Stabilized Zirconia and Yb- and Bi-Doped Gadolinium-Doped Ceria for Highly durable Solid Oxide fuel Cells. International Journal of Precision Engineering and Manufacturing-Green Technology Jul. 2024;11(4):1217–28. https://doi.org/10.1007/s40684-023-00577-6.

[57] A. Hessler-Wyser, Z. Wuillemin, J. A. Schuler, A. Faes, and J. Van herle, "TEM investigation on zirconate formation and chromium poisoning in LSM/YSZ cathode," *J. Mater. Sci.*, vol. 46, no. 13, pp. 4532–4539, Jul. 2011, doi: 10.1007/s10853-011-5347-5.